Riv. Mat. Univ. Parma, Vol. **2** (2011), 1-28

ROMAN VODIČKA and VLADISLAV MANTIČ

On variational formulations for elastic domain decomposition problems solved by SGBEM enforcing coupling conditions in a weak form

Abstract. The solution of Domain Decomposition Boundary Value Problems of linear elasticity is considered. The proposed approach can be deduced either from a potential energy functional expressed in terms of subdomain displacement fields or from a min-max principle of a boundary energy functional expressed in terms of unknown boundary displacement and traction fields. The coupling conditions between two subdomains adjacent to an interface are enforced in a weak form. Two novel features of both functionals are: a distinct role of subdomains lying on the opposite sides of an interface and no requirement of Lagrange multipliers enforcing the coupling conditions. The weak formulation of coupling conditions leads to an easy implementation of SGBEM codes allowing for non-matching meshes along interfaces between subdomains. The presented numerical results confirm an excellent accuracy and convergence behaviour of the numerical solutions, including the cases with non-matching (non-conforming) discretizations of curved interfaces and also with dissimilar materials in subdomains adjacent to an interface.

Keywords. Domain decomposition, variational principles, saddle point, min-max principle, symmetric Galerkin boundary element method, boundary integral equations, non-matching meshes, non-conforming discretization.

Mathematics Subject Classification (2000): 65N55, 74S15, 65N22.

Contents

Received: August 31, 2010; accepted: December 23, 2010.

1 - Introduction

The solution of Boundary Value Problems of linear elasticity using a Domain Decomposition approach (DDBVPs) with non-overlapping subdomains is considered. A new approach to the solution of DDBVPs by Symmetric Galerkin Boundary Element Method (SGBEM) [**3, 16**] has recently been introduced in [**17**]. In this approach the coupling conditions between two subdomains adjacent to a common interface are enforced in a weak form. This feature leads to an easy implementation of SGBEM codes allowing for non-matching meshes along interfaces between subdomains. Previous approaches in SGBEM usually enforced coupling conditions in a strong form and consequently required matching meshes at interfaces [**5, 6, 7, 9, 10, 12, 16**]. Different approaches in collocational BEM allowing for non-conforming meshes were presented, for example, in [**1, 11, 15**].

The present approach is based on two new potential energy functionals for DDBVPs. One of them is expressed in terms of subdomain displacement fields and was introduced in [**17**]. This energy functional generalizes the energy functional studied in the framework of the single domain SGBEM in [**2**]. A novel feature of this functional is a distinct role of the subdomains adjacent to an interface. It was shown that the compatibility along the interface is imposed through the displacement (Dirichlet) boundary conditions on the first subdomain with 'prescribed' displacements of the second subdomain, and the equilibrium along the interface is imposed through the traction (Neumann) boundary conditions on the second subdomain with 'prescribed' tractions of the first subdomain. In this sense the present approach is close to that used in collocational BEM in [**1, 11**].

The other energy functional, expressed in terms of unknown boundary displacements and tractions, corresponds to the functional proposed in [**14**] for single domain problems. This functional was introduced in [**19**] for DDBVP, where also the

governing min-max principle was shown. The min-max principle for this new boundary energy functional provides the same linear system of SGBEM as the aforementioned domain energy functional. A relation between both energy functionals was also deduced in [**19**].

The main focus of this paper is to study numerical properties of the resulting linear system of SGBEM for DDBVPs. The numerical study presented has two aims: first, testing the compatibility and equilibrium of the solution across the interface, straight or curved, and discretized by matching or non-matching meshes and, second, analyzing the behaviour of the solution for an interface between dissimilar materials. With reference to the first aim, a series of simple problems involving zero, constant and linear distributions of interface tractions is considered. The type of problems solved is similar to those usually used for patch tests with finite elements, see [**4, 8**]. With reference to the second aim, a series of problems with either real or somewhat artificial but limit values of linear elastic material parameters is considered.

2 - Domain decomposition

Consider a linear elastic domain $\Omega \subset \mathbb{R}^d$ ($d = 2$ or 3) with a bounded Lipschitz boundary $\Gamma = \partial\Omega$. Let the domain Ω be partitioned, for the sake of simplicity, into two non-overlapping subdomains Ω^A and Ω^B with respective bounded Lipschitz boundaries $\Gamma^A = \partial\Omega^A$ and $\Gamma^B = \partial\Omega^B$, the common part of these boundaries being denoted as Γ_c. Let $\Gamma_u^\eta \subset \Gamma_u$ and $\Gamma_t^\eta \subset \Gamma_t$ ($\eta = A, B$), respectively, denote the boundary parts where the displacements and tractions are prescribed. An example of a bounded domain decomposed into two subdomains can be seen in Figure 1.

Then, a DDBVP for the Navier equation, called also Lamé system, considering vanishing body forces for simplicity, can be defined in the form:

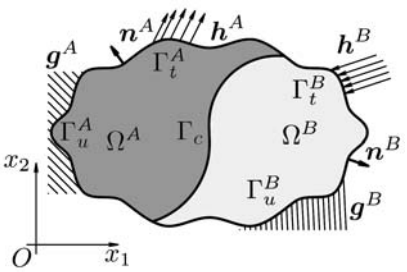

Fig. 1. An example of decomposition of a domain.

$$\text{(1a)} \qquad \operatorname{Div}(\boldsymbol{\sigma}(\boldsymbol{u}^\eta)) = \operatorname{Div}(\boldsymbol{c}^\eta : \boldsymbol{\varepsilon}(\boldsymbol{u}^\eta)) = \boldsymbol{0}, \qquad \text{on } \Omega^\eta, \quad \eta = A, B,$$

$$\text{(1b)} \qquad \boldsymbol{u}^\eta = \boldsymbol{g}^\eta, \text{ on } \Gamma_u^\eta, \quad \boldsymbol{t}^\eta = \boldsymbol{h}^\eta, \qquad \text{on } \Gamma_t^\eta,$$

$$\text{(1c)} \qquad \boldsymbol{u}^A = \boldsymbol{u}^B, \text{ on } \Gamma_c, \quad \boldsymbol{t}^A = -\boldsymbol{t}^B, \qquad \text{on } \Gamma_c,$$

with prescribed boundary conditions in (1b), and with coupling conditions providing compatibility of displacements and equilibrium of tractions (1c). $\boldsymbol{\sigma}(\boldsymbol{u}^\eta)$ and $\boldsymbol{\varepsilon}(\boldsymbol{u}^\eta)$ are respectively the stress and strain tensors given by the displacements $\boldsymbol{u}^\eta$. $\boldsymbol{t}^\eta$ represents tractions on Γ^η calculated from the displacements $\boldsymbol{u}^\eta$ defined in Ω^η *via* traction operator $\boldsymbol{T}_{\boldsymbol{n}^\eta}$, with $\boldsymbol{n}^\eta$ being the unit outward normal vector to Γ^η, see Figure 1. $\boldsymbol{c}^\eta : \boldsymbol{\varepsilon}(\boldsymbol{u}^\eta)$ defines the double contraction of the positive definite fourth rank tensor of the elastic stiffnesses of Ω^η, $\boldsymbol{c}^\eta$, with the strain tensor. Where one subdomain Ω^η is unbounded, suitable decay conditions at infinity should be assumed in addition to (1) for this subdomain.

3 - Two energy functionals for a DDBVP

3.1 - *A functional in terms of subdomain displacements*

The quadratic functional of energy E associated to a DDBVP introduced in [**17**] is an extension of the concept of the augmented potential energy for a single domain, studied in [**2**] in the framework of SGBEM, to DDBVPs.

In the case of two subdomains Ω^η, E can be written as a function of the subdomain displacement fields $\boldsymbol{u}^\eta$ (satisfying the natural conditions of continuity in each subdomain) in the following form:

$$\text{(2)} \quad E(\boldsymbol{u}^A, \boldsymbol{u}^B) = \sum_{\eta=A,B} \left[\frac{1}{2} \int_{\Omega^\eta} \boldsymbol{\sigma}(\boldsymbol{u}^\eta) : \boldsymbol{\varepsilon}(\boldsymbol{u}^\eta) \mathrm{d}V - \int_{\Gamma_t^\eta} \boldsymbol{h}^\eta \boldsymbol{u}^\eta \mathrm{d}S - \int_{\Gamma_u^\eta} \boldsymbol{t}^\eta (\boldsymbol{u}^\eta - \boldsymbol{g}^\eta) \mathrm{d}S \right] - \int_{\Gamma_c} \boldsymbol{t}^A (\boldsymbol{u}^A - \boldsymbol{u}^B) \mathrm{d}S,$$

where $\boldsymbol{t}^\eta = \boldsymbol{T}_{\boldsymbol{n}^\eta}(\boldsymbol{u}^\eta)$. The last integral represents a new term, in comparison with the original single domain formulation in [**2**], defining a form of interface energy associated to both coupling conditions across Γ_c. A noteworthy feature of this interface energy is a non-symmetric role of the subdomains Ω^A and Ω^B in (2).

The critical point of E, giving vanishing (first order) variation of E, represents the solution of the DDBVP (1) when no restrictions are applied to the used virtual displacement fields, see [**17**] for the proof. In addition, the saddle point character of E was shown in [**19**]. Let us choose appropriate virtual displacements $\delta\boldsymbol{u}^\eta$ and evaluate

the variation of the functional E:

$$\begin{aligned}(3)\quad \delta E(\boldsymbol{u}^A,\boldsymbol{u}^B;\delta\boldsymbol{u}^A,\delta\boldsymbol{u}^B) &= \sum_{\eta=A,B}\left[\int_{\Omega^\eta}\boldsymbol{\sigma}(\boldsymbol{u}^\eta):\boldsymbol{\varepsilon}(\delta\boldsymbol{u}^\eta)\mathrm{d}V-\int_{\Gamma_t^\eta}\boldsymbol{h}^\eta\delta\boldsymbol{u}^\eta\mathrm{d}S-\int_{\Gamma_u^\eta}\delta\boldsymbol{t}^\eta(\boldsymbol{u}^\eta-\boldsymbol{g}^\eta)\,\mathrm{d}S-\int_{\Gamma_u^\eta}\boldsymbol{t}^\eta\delta\boldsymbol{u}^\eta\mathrm{d}S\right]\\ &\quad-\int_{\Gamma_c}\delta\boldsymbol{t}^A\big(\boldsymbol{u}^A-\boldsymbol{u}^B\big)\mathrm{d}S-\int_{\Gamma_c}\boldsymbol{t}^A\big(\delta\boldsymbol{u}^A-\delta\boldsymbol{u}^B\big)\mathrm{d}S,\end{aligned}$$

taking into account the symmetry of the double contraction of the stress with strain tensors $\boldsymbol{\sigma}(\boldsymbol{u}^\eta):\boldsymbol{\varepsilon}(\delta\boldsymbol{u}^\eta)=\boldsymbol{\sigma}(\delta\boldsymbol{u}^\eta):\boldsymbol{\varepsilon}(\boldsymbol{u}^\eta)$, and the linearity of the traction operator: $\boldsymbol{t}^\eta+\delta\boldsymbol{t}^\eta=\boldsymbol{\mathcal{T}}_{\boldsymbol{n}^\eta}(\boldsymbol{u}^\eta+\delta\boldsymbol{u}^\eta)$.

It should be stressed that the augmented potential energy functional E itself does not directly provide a variational formulation for a DDBVP discretized by boundary elements, as E is expressed in terms of the domain displacements and requires additional treatment of the volume integral with a special choice of $\delta\boldsymbol{u}^\eta$, see [**2, 17**]. In particular, $\delta\boldsymbol{u}^\eta$ are chosen to satisfy the Navier equation (1a) so that the volume integral in (3) can be eliminated integrating it by parts to obtain the vanishing condition for the variation of the functional E

$$\begin{aligned}(4)\quad 0=\sum_{\eta=A,B}\Bigg[&\int_{\Gamma_t^\eta}\boldsymbol{u}^\eta\delta\boldsymbol{t}^\eta\mathrm{d}S+\int_{\Gamma_u^\eta}\boldsymbol{g}^\eta\delta\boldsymbol{t}^\eta\mathrm{d}S+\int_{\Gamma_c}\boldsymbol{u}^\eta\delta\boldsymbol{t}^\eta\mathrm{d}S-\int_{\Gamma_t^\eta}\boldsymbol{h}^\eta\delta\boldsymbol{u}^\eta\mathrm{d}S\\ &-\int_{\Gamma_u^\eta}\boldsymbol{t}^\eta\delta\boldsymbol{u}^\eta\mathrm{d}S-\int_{\Gamma_c}\boldsymbol{t}^\eta\delta\boldsymbol{u}^\eta\mathrm{d}S\Bigg]-\int_{\Gamma_c}\delta\boldsymbol{t}^A\big(\boldsymbol{u}^A-\boldsymbol{u}^B\big)\mathrm{d}S+\int_{\Gamma_c}\delta\boldsymbol{u}^B\big(\boldsymbol{t}^A+\boldsymbol{t}^B\big)\mathrm{d}S.\end{aligned}$$

The displacements satisfying the Navier equation, together with the pertinent tractions, can be represented by the boundary integral representations defined in the following. Let us introduce the boundary integral operators $\boldsymbol{\mathcal{U}}$, $\boldsymbol{\mathcal{T}}$, $\boldsymbol{\mathcal{T}}^*$ and $\boldsymbol{\mathcal{S}}$. Their definition can be written formally by using a mask operator $\boldsymbol{\mathcal{Z}}$ as

$$(5)\qquad \big(\boldsymbol{\mathcal{Z}}_r^\eta\boldsymbol{w}^\eta\big)(x)=\int_{\Gamma_r^\eta}\boldsymbol{Z}^\eta(x,y)\boldsymbol{w}^\eta(y)\mathrm{d}S_y,$$

where the integral kernel symbol $\boldsymbol{Z}$ is obviously substituted by $\boldsymbol{U}$, $\boldsymbol{T}$, $\boldsymbol{T}^*$ or $\boldsymbol{S}$, respectively. The integral kernel $\boldsymbol{U}^\eta(x,y)=\boldsymbol{U}^{\eta T}(y,x)$ represents the fundamental solution in displacements of the Navier equation, and the other kernels represent its derivatives, namely $\boldsymbol{T}^{\eta*}(x,y)=\boldsymbol{\mathcal{T}}_{\boldsymbol{n}^\eta(x)}\boldsymbol{U}^\eta(x,y)$ with $\boldsymbol{T}^\eta(x,y)=\boldsymbol{T}^{\eta*\,T}(y,x)$ and $\boldsymbol{S}^\eta(x,y)=\boldsymbol{S}^{\eta T}(y,x)=\boldsymbol{\mathcal{T}}_{\boldsymbol{n}^\eta(x)}\boldsymbol{T}^\eta(x,y)$, superscript T denoting the transposed matrix.

Recall that some of the integrals are evaluated in the sense of the Cauchy principal value and Hadamard finite part, where required, due to the high order singularities of the kernels $\boldsymbol{T}^{\eta}$ and $\boldsymbol{T}^{\eta *}$ (strongly singular) and $\boldsymbol{S}^{\eta}$ (hyper-singular). The representation formulae restricted by a limit-to-the-boundary procedure to the boundaries of the subdomains can be written in the form:

$$\delta \boldsymbol{u}^{\eta} = \boldsymbol{\mathcal{U}}^{\eta} \boldsymbol{\varphi}^{\eta} - \boldsymbol{\mathcal{T}}^{\eta} \boldsymbol{\psi}^{\eta} + \boldsymbol{\mathcal{C}}^{\eta}_{tc} \boldsymbol{\psi}^{\eta}, \qquad \delta \boldsymbol{t}^{\eta} = \boldsymbol{\mathcal{T}}^{\eta *} \boldsymbol{\varphi}^{\eta} - \boldsymbol{\mathcal{S}}^{\eta} \boldsymbol{\psi}^{\eta} + \boldsymbol{\mathcal{C}}^{\eta}_{uc} \boldsymbol{\varphi}^{\eta}, \tag{6}$$

where $\boldsymbol{\mathcal{C}}^{\eta}_{r} = 1/2\,\boldsymbol{\mathcal{I}}$ on smooth parts of Γ^{η}_{r} and vanishes on $\Gamma^{\eta} \setminus \Gamma^{\eta}_{r}$. The subscript r denotes the boundary part according to the boundary conditions (1b) and interface conditions (1c). Thus r can be u, t, c or any of their combinations (say, $\Gamma^{\eta}_{uc} = \Gamma^{\eta}_{u} \cup \Gamma_{c}$, *etc.*). As the boundary potentials $\boldsymbol{\varphi}$ and $\boldsymbol{\psi}$ are not uniquely defined, see [**17**], they can be set to be advantageous with the present formulation of DDBVP. The appropriate choice includes following conditions

$$\boldsymbol{\varphi}^{\eta} = \boldsymbol{0}, \quad \text{on } \Gamma^{\eta}_{t}, \qquad \boldsymbol{\varphi}^{A} = \delta \boldsymbol{t}^{A}_{c}, \quad \text{on } \Gamma_{c}, \tag{7a}$$

$$\boldsymbol{\psi}^{\eta} = \boldsymbol{0}, \quad \text{on } \Gamma^{\eta}_{u}, \qquad \boldsymbol{\psi}^{B} = \delta \boldsymbol{u}^{B}_{c}, \quad \text{on } \Gamma_{c}. \tag{7b}$$

The representations (6) together with the conditions (7) can be substituted into (4). The order of the integrations (one from the representations, one from the functional) can be interchanged and the dot products can be generalized by the symbol of L_2-duality pairing over the boundary Γ^{η}_{r}, *i. e.* : $\langle \boldsymbol{v}^{\eta}, \boldsymbol{w}^{\eta} \rangle_{r} = \int\limits_{\Gamma^{\eta}_{r}} \boldsymbol{v}^{\eta} \boldsymbol{w}^{\eta} \mathrm{d}S$. The obtained system of boundary integral equations takes the following form:

$$\begin{aligned} 0 = - \sum_{\eta = A,B} \Big[& \big\langle \boldsymbol{\varphi}^{\eta}, \big(\boldsymbol{\mathcal{U}}^{\eta}_{uc} \boldsymbol{t}^{\eta} - \boldsymbol{\mathcal{T}}^{\eta}_{tc} \boldsymbol{u}^{\eta} + \boldsymbol{\mathcal{U}}^{\eta}_{t} \boldsymbol{h}^{\eta} - \boldsymbol{\mathcal{T}}^{\eta}_{u} \boldsymbol{g}^{\eta} - \boldsymbol{\mathcal{C}}^{\eta}_{u} \boldsymbol{g}^{\eta} \big) \big\rangle_{u} \\ & + \big\langle \boldsymbol{\psi}^{\eta}, \big(- \boldsymbol{\mathcal{T}}^{\eta *}_{uc} \boldsymbol{t}^{\eta} + \boldsymbol{\mathcal{S}}^{\eta}_{tc} \boldsymbol{u}^{\eta} - \boldsymbol{\mathcal{T}}^{\eta *}_{t} \boldsymbol{h}^{\eta} + \boldsymbol{\mathcal{C}}^{\eta}_{t} \boldsymbol{h}^{\eta} + \boldsymbol{\mathcal{S}}^{\eta}_{u} \boldsymbol{g}^{\eta} \big) \big\rangle_{t} \Big] \\ & - \Big\langle \boldsymbol{\varphi}^{A}, \Big(\boldsymbol{\mathcal{U}}^{A}_{uc} \boldsymbol{t}^{A} - \boldsymbol{\mathcal{T}}^{A}_{tc} \boldsymbol{u}^{A} - \boldsymbol{\mathcal{C}}^{A}_{c} \boldsymbol{u}^{A} + \big(\boldsymbol{u}^{A} - \boldsymbol{u}^{B} \big) + \boldsymbol{\mathcal{U}}^{A}_{t} \boldsymbol{h}^{A} - \boldsymbol{\mathcal{T}}^{A}_{u} \boldsymbol{g}^{A} \Big) \Big\rangle_{c} \\ & - \Big\langle \boldsymbol{\psi}^{A}, \Big(- \boldsymbol{\mathcal{T}}^{A *}_{uc} \boldsymbol{t}^{A} + \boldsymbol{\mathcal{C}}^{A}_{c} \boldsymbol{t}^{A} + \boldsymbol{\mathcal{S}}^{A}_{tc} \boldsymbol{u}^{A} - \boldsymbol{\mathcal{T}}^{A *}_{t} \boldsymbol{h}^{A} + \boldsymbol{\mathcal{S}}^{A}_{u} \boldsymbol{g}^{A} \Big) \Big\rangle_{c} \\ & - \Big\langle \boldsymbol{\varphi}^{B}, \Big(\boldsymbol{\mathcal{U}}^{B}_{uc} \boldsymbol{t}^{B} - \boldsymbol{\mathcal{T}}^{B}_{tc} \boldsymbol{u}^{B} - \boldsymbol{\mathcal{C}}^{B}_{c} \boldsymbol{u}^{B} + \boldsymbol{\mathcal{U}}^{B}_{t} \boldsymbol{h}^{B} - \boldsymbol{\mathcal{T}}^{B}_{u} \boldsymbol{g}^{B} \Big) \Big\rangle_{c} \\ & - \Big\langle \boldsymbol{\psi}^{B}, \Big(- \boldsymbol{\mathcal{T}}^{B *}_{uc} \boldsymbol{t}^{B} + \boldsymbol{\mathcal{C}}^{B}_{c} \boldsymbol{t}^{B} + \boldsymbol{\mathcal{S}}^{B}_{tc} \boldsymbol{u}^{B} - \big(\boldsymbol{t}^{A} + \boldsymbol{t}^{B} \big) - \boldsymbol{\mathcal{T}}^{B *}_{t} \boldsymbol{h}^{B} + \boldsymbol{\mathcal{S}}^{B}_{u} \boldsymbol{g}^{B} \Big) \Big\rangle_{c}. \end{aligned} \tag{8}$$

As expected, the final system shows the distinct role of the two subdomains Ω^{A} and Ω^{B} adjacent to the interface Γ_{c}.

3.2 - *A functional in terms of boundary displacements and tractions*

A quadratic functional of energy Π associated to a DDBVP expressed in terms of the unknown displacements $\boldsymbol{u}$ and tractions $\boldsymbol{t}$ defined along the subdomain bound-

aries will be introduced in this section. In the case of one domain, an energy functional of this kind, yielding a min-max principle for the unknown displacements and tractions defined on the domain boundary, was proposed and studied in [**14**]. The advantage of such a formulation for the application of SGBEM is obvious. A generalization of this functional to the case of a DDBVP (with two subdomains) can be written in the following form:

$$\Pi(\boldsymbol{u}^A,\boldsymbol{u}^B,\boldsymbol{t}^A,\boldsymbol{t}^B) = -\sum_{\eta=A,B}\left[\frac{1}{2}\langle \boldsymbol{t}^\eta,\boldsymbol{\mathcal{U}}^\eta_{uc}\boldsymbol{t}^\eta\rangle_{uc}+\frac{1}{2}\langle \boldsymbol{u}^\eta,\boldsymbol{\mathcal{S}}^\eta_{tc}\boldsymbol{u}^\eta\rangle_{tc}-\langle \boldsymbol{t}^\eta,\boldsymbol{\mathcal{T}}^\eta_{tc}\boldsymbol{u}^\eta\rangle_{uc}\right] \tag{9}$$

$$-\frac{1}{2}\left[\langle \boldsymbol{t}^A,\boldsymbol{u}^A-\boldsymbol{u}^B\rangle_c-\langle \boldsymbol{u}^B,\boldsymbol{t}^A+\boldsymbol{t}^B\rangle_c\right]-\sum_{\eta=A,B}\left[\langle \boldsymbol{t}^\eta,\bar{\boldsymbol{g}}^\eta\rangle_{uc}+\langle \boldsymbol{u}^\eta,\bar{\boldsymbol{h}}^\eta\rangle_{tc}\right],$$

where L_2-duality pairing $\langle,\rangle_r$ over the boundary Γ^η_r and the boundary integral operators $\boldsymbol{\mathcal{U}}$, $\boldsymbol{\mathcal{T}}$ and $\boldsymbol{\mathcal{S}}$ were introduced in Section 3.1.

The unknown functions $\boldsymbol{u}^\eta$ and $\boldsymbol{t}^\eta$ are assumed to satisfy the natural continuity conditions at each subdomain, $\boldsymbol{u}^\eta$ being a continuous extension of the displacement boundary condition $\boldsymbol{g}^\eta$ to Γ^η_{tc}. The functions with bar (defined almost everywhere on the boundary) represent the prescribed boundary data in the following way:

$$\bar{\boldsymbol{g}}^\eta=\boldsymbol{\mathcal{U}}^\eta_t\boldsymbol{h}^\eta-\boldsymbol{\mathcal{T}}^\eta_u\boldsymbol{g}^\eta-\boldsymbol{\mathcal{C}}^\eta_u\boldsymbol{g}^\eta,\ \text{on } \Gamma^\eta_{uc},\quad \bar{\boldsymbol{h}}^\eta=-\boldsymbol{\mathcal{T}}^{\eta*}_t\boldsymbol{h}^\eta+\boldsymbol{\mathcal{S}}^\eta_u\boldsymbol{g}^\eta+\boldsymbol{\mathcal{C}}^\eta_t\boldsymbol{h}^\eta,\ \text{on } \Gamma^\eta_{tc}. \tag{10}$$

The terms with the subscript c in (9) represent new terms, in comparison with the original single domain formulation in [**14**], defining a form of interface energy associated to both coupling conditions across Γ_c. As in (2), here also the noteworthy feature of this interface energy is the distinct role of the subdomains Ω^A and Ω^B.

Let us choose virtual displacements $\delta\boldsymbol{u}^\eta$ (being able to be continuously extended to Γ^η) and virtual tractions $\delta\boldsymbol{t}^\eta$. The first order variation, $\delta\Pi$, can be written in the form:

$$\begin{aligned}
&\delta\Pi(\boldsymbol{u}^A,\boldsymbol{u}^B,\boldsymbol{t}^A,\boldsymbol{t}^B;\delta\boldsymbol{u}^A,\delta\boldsymbol{u}^B,\delta\boldsymbol{t}^A,\delta\boldsymbol{t}^B) \\
&\quad=-\sum_{\eta=A,B}\Big[\big\langle\delta\boldsymbol{t}^\eta,\big(\boldsymbol{\mathcal{U}}^\eta_{uc}\boldsymbol{t}^\eta-\boldsymbol{\mathcal{T}}^\eta_{tc}\boldsymbol{u}^\eta+\boldsymbol{\mathcal{U}}^\eta_t\boldsymbol{h}^\eta-\boldsymbol{\mathcal{T}}^\eta_u\boldsymbol{g}^\eta-\boldsymbol{\mathcal{C}}^\eta_u\boldsymbol{g}^\eta\big)\big\rangle_u \\
&\qquad\qquad+\big\langle\delta\boldsymbol{u}^\eta,\big(-\boldsymbol{\mathcal{T}}^{\eta*}_{uc}\boldsymbol{t}^\eta+\boldsymbol{\mathcal{S}}^\eta_{tc}\boldsymbol{u}^\eta-\boldsymbol{\mathcal{T}}^{\eta*}_t\boldsymbol{h}^\eta+\boldsymbol{\mathcal{C}}^\eta_t\boldsymbol{h}^\eta+\boldsymbol{\mathcal{S}}^\eta_u\boldsymbol{g}^\eta\big)\big\rangle_t\Big] \\
&\quad-\Big\langle\delta\boldsymbol{t}^A,\Big(\boldsymbol{\mathcal{U}}^A_{uc}\boldsymbol{t}^A-\boldsymbol{\mathcal{T}}^A_{tc}\boldsymbol{u}^A-\boldsymbol{\mathcal{C}}^A_c\boldsymbol{u}^A+\underline{(\boldsymbol{u}^A-\boldsymbol{u}^B)}+\boldsymbol{\mathcal{U}}^A_t\boldsymbol{h}^A-\boldsymbol{\mathcal{T}}^A_u\boldsymbol{g}^A\Big)\Big\rangle_c \\
&\qquad-\Big\langle\delta\boldsymbol{u}^A,\Big(-\boldsymbol{\mathcal{T}}^{A*}_{uc}\boldsymbol{t}^A+\boldsymbol{\mathcal{C}}^A_c\boldsymbol{t}^A+\boldsymbol{\mathcal{S}}^A_{tc}\boldsymbol{u}^A-\boldsymbol{\mathcal{T}}^{A*}_t\boldsymbol{h}^A+\boldsymbol{\mathcal{S}}^A_u\boldsymbol{g}^A\Big)\Big\rangle_c \\
&\qquad\quad-\Big\langle\delta\boldsymbol{t}^B,\Big(\boldsymbol{\mathcal{U}}^B_{uc}\boldsymbol{t}^B-\boldsymbol{\mathcal{T}}^B_{tc}\boldsymbol{u}^B-\boldsymbol{\mathcal{C}}^B_c\boldsymbol{u}^B+\boldsymbol{\mathcal{U}}^B_t\boldsymbol{h}^B-\boldsymbol{\mathcal{T}}^B_u\boldsymbol{g}^B\Big)\Big\rangle_c \\
&\quad-\Big\langle\delta\boldsymbol{u}^B,\Big(-\boldsymbol{\mathcal{T}}^{B*}_{uc}\boldsymbol{t}^B+\boldsymbol{\mathcal{C}}^B_c\boldsymbol{t}^B+\boldsymbol{\mathcal{S}}^B_{tc}\boldsymbol{u}^B-\underline{(\boldsymbol{t}^A+\boldsymbol{t}^B)}-\boldsymbol{\mathcal{T}}^{B*}_t\boldsymbol{h}^B+\boldsymbol{\mathcal{S}}^B_u\boldsymbol{g}^B\Big)\Big\rangle_c.
\end{aligned} \tag{11}$$

The condition for vanishing $\delta\Pi$ represents in fact the variational formulation of the symmetric system of BIEs together with the coupling conditions deduced in [**17**] and studied in [**19**]. Thus, the functions $\tilde{\boldsymbol{u}}^\eta$ and $\tilde{\boldsymbol{t}}^\eta$, defining a critical point of Π, represent also a solution of this system of BIEs and coupling conditions. It can also be easily seen that a solution of the DDBVP (1) represents a critical point of Π, as each expression in parentheses of (11) vanishes because the solution of DDBVP satisfies the well-known displacement and traction BIEs [**3, 6, 16**] and the coupling conditions of compatibility and equilibrium (underlined terms in (11)). In fact, the system of BIE (11) is the same as that obtained from the functional E (2), *c.f.* (8).

Finally, it should be stressed that the stationary point of the functional Π is its saddle point, see [**19**], and it can be found using the following *boundary min-max principle*, minimizing Π with respect to displacements and maximizing its value with respect to tractions:

$$\min_{\boldsymbol{u}^\eta}\max_{\boldsymbol{t}^\eta}\Pi\left(\boldsymbol{u}^A,\boldsymbol{u}^B,\boldsymbol{t}^A,\boldsymbol{t}^B\right)=\max_{\boldsymbol{t}^\eta}\min_{\boldsymbol{u}^\eta}\Pi\left(\boldsymbol{u}^A,\boldsymbol{u}^B,\boldsymbol{t}^A,\boldsymbol{t}^B\right)=\Pi(\tilde{\boldsymbol{u}}^A,\tilde{\boldsymbol{u}}^B,\tilde{\boldsymbol{t}}^A,\tilde{\boldsymbol{t}}^B). \tag{12}$$

This explicit min-max statement of the problem gives to the functional Π another advantage with respect to the domain based functional E if the numerical solution by boundary elements is considered.

4 - Discretization by boundary elements

Let us introduce an approximation of the boundary displacements and tractions by continuous linear boundary elements [**13**] (allowing discontinuities of tractions at the junctions of boundary elements if required):

$$\boldsymbol{u}^\eta(x)=\sum_k \boldsymbol{N}^\eta_{\boldsymbol{u}k}(x)\mathsf{u}^\eta_k,\quad \boldsymbol{t}^\eta(x)=\sum_k \boldsymbol{N}^\eta_{\boldsymbol{t}k}(x)\mathsf{t}^\eta_k, \tag{13}$$

where $\boldsymbol{N}^\eta_{\boldsymbol{u}k}(x)$ and $\boldsymbol{N}^\eta_{\boldsymbol{t}k}(x)$, respectively, are diagonal matrices containing the shape functions of displacements and tractions associated to node k at Γ^η, and u^η_k and t^η_k, respectively, are vectors containing the components of the displacement and traction vector at the node k. Let u^η and t^η, respectively, denote the vectors containing all unknown nodal displacements and all unknown nodal tractions associated to Γ^η. Let the subvectors of the nodal unknowns associated to the boundary parts Γ^η_u, Γ^η_t and Γ_c, respectively, be distinguished by the same subscripts u, t and c, omitting the superscript η refers to the nodal data for all the subdomains. Moreover, following the notation introduced in (5) and (9), $\mathbf{Z}$-matrices can be introduced:

$$(\mathbf{Z}^\eta_{rs})_{kl}=\left\langle \boldsymbol{N}^\eta_{\boldsymbol{z}_r k},\boldsymbol{Z}^\eta_s\boldsymbol{N}^\eta_{\boldsymbol{z}_s l}\right\rangle_r, \tag{14}$$

with $\boldsymbol{z}_r$ and $\boldsymbol{z}_s$, along with the nature of the integral kernel, determining the correct choice of the nodal shape functions $\boldsymbol{N}^{\eta}_{\boldsymbol{u}k}$ and $\boldsymbol{N}^{\eta}_{\boldsymbol{t}k}$. Similarly, the prescribed boundary data, calculated from (10), introduce the terms

$$(\bar{\mathsf{g}}^{\eta}_r)_k = \left\langle \boldsymbol{N}^{\eta}_{\boldsymbol{t}k}, \bar{\boldsymbol{g}}^{\eta} \right\rangle_r, \qquad (\bar{\mathsf{h}}^{\eta}_r)_k = \left\langle \boldsymbol{N}^{\eta}_{\boldsymbol{u}k}, \bar{\boldsymbol{h}}^{\eta} \right\rangle_r. \tag{15}$$

All the prescribed nodal boundary data associated to Γ^{η} are, with an obvious pertinency, denoted $\bar{\mathsf{g}}^{\eta}$ and $\bar{\mathsf{h}}^{\eta}$, possibly with a subscript u, t or c or without the superscript η.

Additionally, two kinds of mass matrices M are introduced, in order to correctly discretize the free and interface terms of Π. The matrices are generated as follows:

$$(\mathsf{M}^{\eta}_{rr})_{kl} = \left\langle \boldsymbol{N}^{\eta}_{\boldsymbol{t}k}, \boldsymbol{N}^{\eta}_{\boldsymbol{u}l} \right\rangle_r, \qquad (\mathsf{M}^{AB}_{cc})_{kl} = \left\langle \boldsymbol{N}^{A}_{\boldsymbol{t}k}, \boldsymbol{N}^{B}_{\boldsymbol{u}l} \right\rangle_c. \tag{16}$$

It should be stressed that the mass matrices do not have to be square as the number of nodes for displacement can be different from that for tractions. Moreover, the coupled meshes from both subdomains along Γ_c can be independent of each other.

The variational formulations of the BIE systems obtained from both functionals E (2) and Π (9) are in fact the same as can be seen by a comparison of (8) and (11). The system of algebraic equations is then also the same and it reads:

$$\mathsf{A}\mathsf{x} = \mathsf{b} \tag{17}$$

where

$$\begin{aligned} \mathsf{x} &= \left(\mathsf{t}^A_u, \mathsf{u}^A_t, \mathsf{t}^A_c, \mathsf{u}^A_c, \mathsf{t}^B_u, \mathsf{u}^B_t, \mathsf{t}^B_c, \mathsf{u}^B_c\right)^T, \\ \mathsf{b} &= \left(\bar{\mathsf{g}}^A_u, \bar{\mathsf{h}}^A_t, \bar{\mathsf{g}}^A_c, \bar{\mathsf{h}}^A_c, \bar{\mathsf{g}}^B_u, \bar{\mathsf{h}}^B_t, \bar{\mathsf{g}}^B_c, \bar{\mathsf{h}}^B_c\right)^T \end{aligned} \tag{18}$$

and

$$\mathsf{A} = \begin{pmatrix} -\mathsf{U}^A_{uu} & \mathsf{T}^A_{ut} & -\mathsf{U}^A_{uc} & \mathsf{T}^A_{uc} & \mathsf{0} & \mathsf{0} & \mathsf{0} & \mathsf{0} \\ \mathsf{T}^{A*}_{tu} & -\mathsf{S}^A_{tt} & \mathsf{T}^{A*}_{tc} & -\mathsf{S}^A_{tc} & \mathsf{0} & \mathsf{0} & \mathsf{0} & \mathsf{0} \\ -\mathsf{U}^A_{cu} & \mathsf{T}^A_{ct} & -\mathsf{U}^A_{cc} & -\frac{1}{2}\mathsf{M}^A_{cc}+\mathsf{T}^A_{cc} & \mathsf{0} & \mathsf{0} & \mathsf{0} & \mathsf{M}^{AB}_{cc} \\ \mathsf{T}^{A*}_{cu} & -\mathsf{S}^A_{ct} & -\frac{1}{2}\mathsf{M}^{A\,T}_{cc}+\mathsf{T}^{A*}_{cc} & -\mathsf{S}^A_{cc} & \mathsf{0} & \mathsf{0} & \mathsf{0} & \mathsf{0} \\ \mathsf{0} & \mathsf{0} & \mathsf{0} & \mathsf{0} & -\mathsf{U}^B_{uu} & \mathsf{T}^B_{ut} & -\mathsf{U}^B_{uc} & \mathsf{T}^B_{uc} \\ \mathsf{0} & \mathsf{0} & \mathsf{0} & \mathsf{0} & \mathsf{T}^{B*}_{tu} & -\mathsf{S}^B_{tt} & \mathsf{T}^{B*}_{tc} & -\mathsf{S}^B_{tc} \\ \mathsf{0} & \mathsf{0} & \mathsf{0} & \mathsf{0} & -\mathsf{U}^B_{cu} & \mathsf{T}^B_{ct} & -\mathsf{U}^B_{cc} & \frac{1}{2}\mathsf{M}^B_{cc}+\mathsf{T}^B_{cc} \\ \mathsf{0} & \mathsf{0} & \mathsf{M}^{AB\,T}_{cc} & \mathsf{0} & \mathsf{T}^{B*}_{cu} & -\mathsf{S}^B_{ct} & \frac{1}{2}\mathsf{M}^{B\,T}_{cc}+\mathsf{T}^{B*}_{cc} & -\mathsf{S}^B_{cc} \end{pmatrix}. \tag{19}$$

5 - Numerical examples

5.1 - *Problem configurations and discretizations*

Two different kinds of problems are solved and discussed. In the first kind of test problems, transfer of the solution through an interface for matching and non-matching meshes is compared. Simple problems resulting in a vanishing, constant and linear distributions of interface tractions are considered. In particular, uniaxial tension of a bar and pure bending of a beam are considered as the test problems, see Figure 2 with dimensions given in millimeters, considering the state of plane strain. The types of problems are similar to those typically used for patch tests with finite elements [4, 8].

Two meshes are considered: a coarse uniform mesh with element length 100 mm denoted by the key 'M1' and a fine uniform mesh with element length 25 mm, the key 'M2'. For both meshes, matching (conforming) and non-matching (non-conforming) disretizations ('C' and 'N' option, respectively) of the interface Γ_c are compared. A non-matching mesh is generated by partitioning each interface boundary element pertaining to Ω_B into four elements, forming a '1:4' mesh pattern along Γ_c.

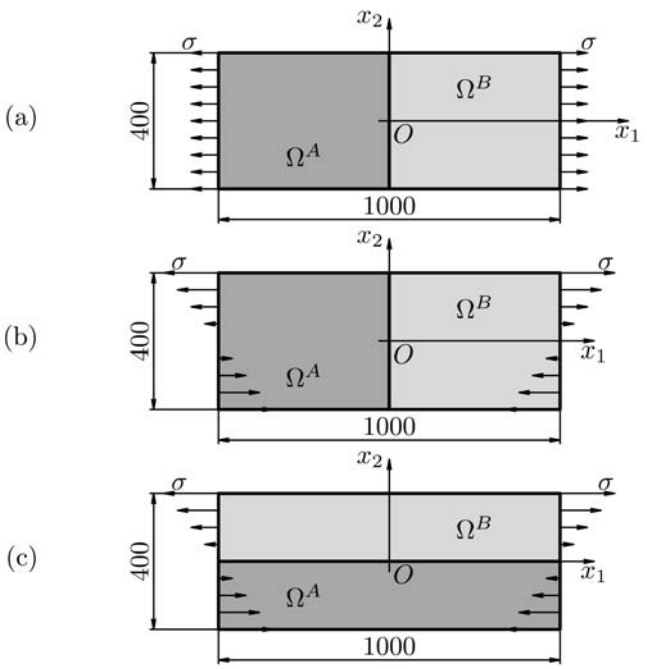

Fig. 2. The test problems configurations: (a) Bar, (b) Beam_V, (c) Beam_L.

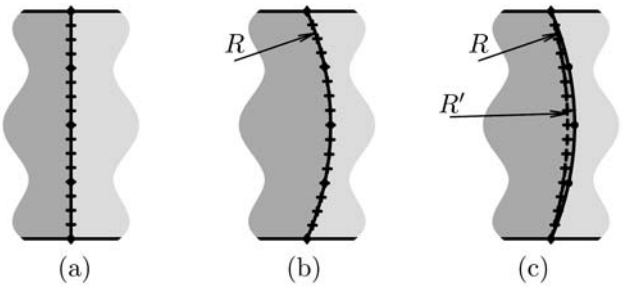

Fig. 3. The interface Γ_c and its discretizations in the cases Bar and Beam_V: (a) A straight line (L), (b) An arc (A), (c) Two distinct arcs (D) with a subdomain overlapping.

With the objective to study the sensitivity of the numerical results on slight interface perturbations the following cases are also considered. The vertical interface Γ_c in the cases Bar and Beam_V defined in Figure 2 is slightly perturbed from its original straight form to the shape of a circular arc with radius R=2000 mm, or two distinct arcs with radii R=2000 mm and R'=2010 mm on the Ω^A and Ω^B sides, respectively, for the mesh M1, and R=2000 mm and R'=2002.5 mm on the Ω^A and Ω^B sides, respectively, for the mesh M2, see Figure 3. In what follows, these three modifications are marked as 'L' (straight line), 'A' (arc) and 'D' (distinct arcs), respectively. The cases 'L' and 'A' represent geometrically conforming cases, and the case 'D' represents a geometrically non-conforming case with some overlapping of the subdomains Ω^A and Ω^B.

The magnitudes of applied load are $\sigma = 1$ MPa for the tension problem and $\sigma = 8$MPa as maximum tensile stress for the bending problem. The elastic material properties of both subdomains Ω^A and Ω^B are the same and corresponding to steel, $E = 2 \times 10^5$ MPa and $\nu = 0.3$.

The second kind of test problems includes a bi-material interface. It is a problem of an infinite fibre with a circular cross section embedded in an unbounded matrix subjected to a transverse load at infinity, see Figure 4(a). A plain strain state is considered. However, the particular code used in testing is not suitable for solving the problems with unbounded domains. Therefore, an outer contour of the matrix had to be chosen with a given load corresponding to the tractions of the original solution, which is shown in Figure 4(b).

The analysis of numerical results is again focused on the comparison of the interface results for matching and non-matching discretizations. The boundary element meshes are uniform, starting with 12 elements along the inclusion boundary, the mesh M1, with three additional refinements (M2, M3, M4), each with the double number of the elements. The non-matching interface meshes are obtained by dis-

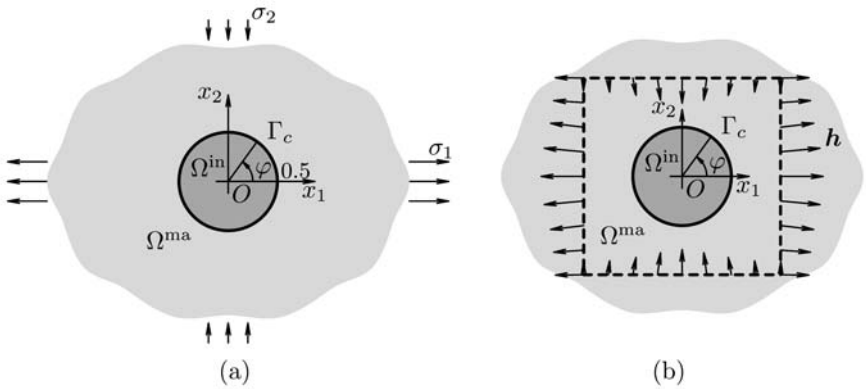

Fig. 4. The inclusion problem: (a) original definition, (b) actually solved configuration.

cretizing Γ_c by 28 elements in the mesh M1 on the side of the matrix domain $\Omega^{\rm ma}$, forming in this way a '3:7' mesh pattern.

The applied load is a combination of tension in the x_1 direction and compression in the x_2 direction, their magnitudes being σ_1=2 MPa and σ_2=1 MPa. The material properties of the subdomains Ω^A=$\Omega^{\rm in}$ and Ω^B=$\Omega^{\rm ma}$ are chosen to correspond to the typical glass-fiber epoxy-matrix composite materials: $E^{\rm ma}$=2.79×10^3 MPa, $\nu^{\rm ma}$=0.33 and $E^{\rm in}$=7.08×10^4 MPa, $\nu^{\rm in}$=0.22. Another choice of the material properties considered in the present work is a limit case, which includes an almost rigid fiber (in comparison to the matrix) and an almost incompressible matrix. Their values have been chosen as follows: $E^{\rm in}$=10^3×$E^{\rm ma}$=1×10^6 MPa, $\nu^{\rm ma}$=0.499, $\nu^{\rm in}$=0.0.

The solution for stresses can be deduced from the Airy stress function, see [**20, 21**], which is expressed in polar coordinates by radial functions and periodic functions containing $\cos 2\varphi$ only, due to symmetry conditions. The interface tractions can be computed from the homogeneous stress state in the inclusion given by

$$\begin{aligned} \sigma_{11} &= \frac{1}{2}\frac{1+\alpha}{1+\beta}\left[\frac{2+\alpha-\beta}{1+\alpha-2\beta}(\sigma_1+\sigma_2)-2\sigma_2\right], \\ \sigma_{22} &= \frac{1}{2}\frac{1+\alpha}{1+\beta}\left[\frac{2+\alpha-\beta}{1+\alpha-2\beta}(\sigma_1+\sigma_2)-2\sigma_1\right], \quad \sigma_{12}=0, \end{aligned} \tag{20}$$

where α and β are Dundurs bi-material dimensionless parameters which can be expressed as

$$\begin{aligned} \alpha &= \frac{E^{\rm in}(1-(\nu^{\rm ma})^2)-E^{\rm ma}(1-(\nu^{\rm in})^2)}{E^{\rm in}(1-(\nu^{\rm ma})^2)+E^{\rm ma}(1-(\nu^{\rm in})^2)}, \\ \beta &= \frac{E^{\rm in}(\frac{1}{2}-\nu^{\rm ma})(1+\nu^{\rm ma})-E^{\rm ma}(\frac{1}{2}-\nu^{\rm in})(1+\nu^{\rm in})}{E^{\rm in}(1-(\nu^{\rm ma})^2)+E^{\rm ma}(1-(\nu^{\rm in})^2)}. \end{aligned} \tag{21}$$

Assuming natural symmetry conditions in this problem (x_1 and x_2 being symmetry axes), the Airy stress function also gives a unique displacement solution.

5.2 - *Error evaluation*

Present analysis is concerned with the behaviour of the numerical solutions obtained along the interface. Let the numerical solution of a problem be denoted in generic way as $\boldsymbol{z}_n$ and the analytical one as $\boldsymbol{z}_a$.

The relative error, which is simply the difference $\boldsymbol{z}_n(x) - \boldsymbol{z}_a(x),\ x \in \Gamma_c$, divided by the max-norm of $\boldsymbol{z}_a$ obtained on the contour Γ pertinent to the originally solved problem, is presented together with **the interface difference** $\boldsymbol{z}_n^A(x) - \boldsymbol{z}_n^B(x)$, $x \in \Gamma_c$, divided by the same value. Both are naturally approximated linearly between the nodes in view of the used discretization, Section 4. Note that the interface difference appears due to the non-conformity of meshes on both sides of the interface Γ_c.

The following two discretized error norms have been chosen to characterize the convergence behaviour of the method along Γ_c for the inclusion-matrix problem, the integral L_2-norm and the maximum norm. The former is expected to present a regular convergence behaviour, whereas the latter is of major interest for engineers, who are typically interested in maximum values of displacements or stresses, respectively, applied in the so-called 'stiffness' and 'strength' criteria.

Integral L_2 norm of error defined as:

$$\|\boldsymbol{z}_n - \boldsymbol{z}_a\|_{L_2} = \sqrt{\int_{\Gamma_c} \sum_{l=1}^{2} \big(z_{nl}(x) - z_{al}(x)\big)^2 \mathrm{d}S_x} \tag{22}$$

is approximated using the Simpson rule along the discretized Γ_c.

Maximum norm of error is defined as the maximum of absolute error achieved over all nodes for a particular mesh:

$$\|\boldsymbol{z}_n - \boldsymbol{z}_a\|_{\mathrm{MAX}} = \max_{x_i - \mathrm{node}} \max_{l=1,2} \big|z_{nl}(x_i) - z_{al}(x_i)\big|. \tag{23}$$

Convergence rate for an h refinement is defined as the number β for which exists a constant q such that the relation

$$\|\boldsymbol{z}_n^N - \boldsymbol{z}_a\| \approx q \cdot N^{-\beta} \|\boldsymbol{z}_a\|, \tag{24}$$

holds for a selected error norm, N giving the characteristic number of elements of a mesh and $\boldsymbol{z}_n^N$ giving the numerical solution for this particular mesh. The parameters β and q are obtained by least square fitting in log-log scale, for which the correlation coefficient r is also calculated.

5.3 - *Tests of equilibrium and compatibility* (*Patch tests*)

First, transfer of a constant traction solution and a linear displacement solution across an interface in the simple tension problem of a bar, see Figure 2(a), is studied.

The left plot in Figure 5 shows that the unit constant traction, t_1, is transferred through a straight interface correctly even when the meshes do not match. If the interface is curved, but geometrically both sides of the interface are conforming, the errors do not vanish due to approximation of the curved interface geometry by linear boundary elements. The magnitude and also the difference of the errors are with no surprise larger for geometrically not conforming interface approximated by different curves from both sides, the case D. The obtained errors for this case are plotted divided by 10 in order to facilitate an easy visual comparison with the other error distributions.

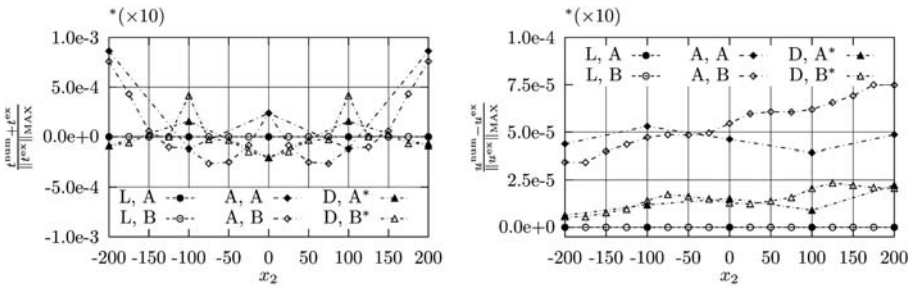

Fig. 5. Bar, simple tension problem. Relative errors of interface tractions t_1 and displacements u_2, mesh M1, non-matching meshes.

The difference of the obtained results for the tractions t_1 on both sides of the interface is shown in Figure 6. With reference to coarser meshes M1, see the left column of Figure 6, a difference between the matching and non-matching meshes can be observed. The solution is transferred correctly through the straight line, the case L, not depending whether the interface meshes match or not. However, for the curved discretized interface, case A, a difference appears. The traction solution is almost constant along the interface, thus approximation with more linear elements, although only along one side of the interface, may provide a more accurate solution for the non-matching mesh. The slightly different radii of curvature of both sides of the discretized interface, case D, make the interface solution difference more significant.

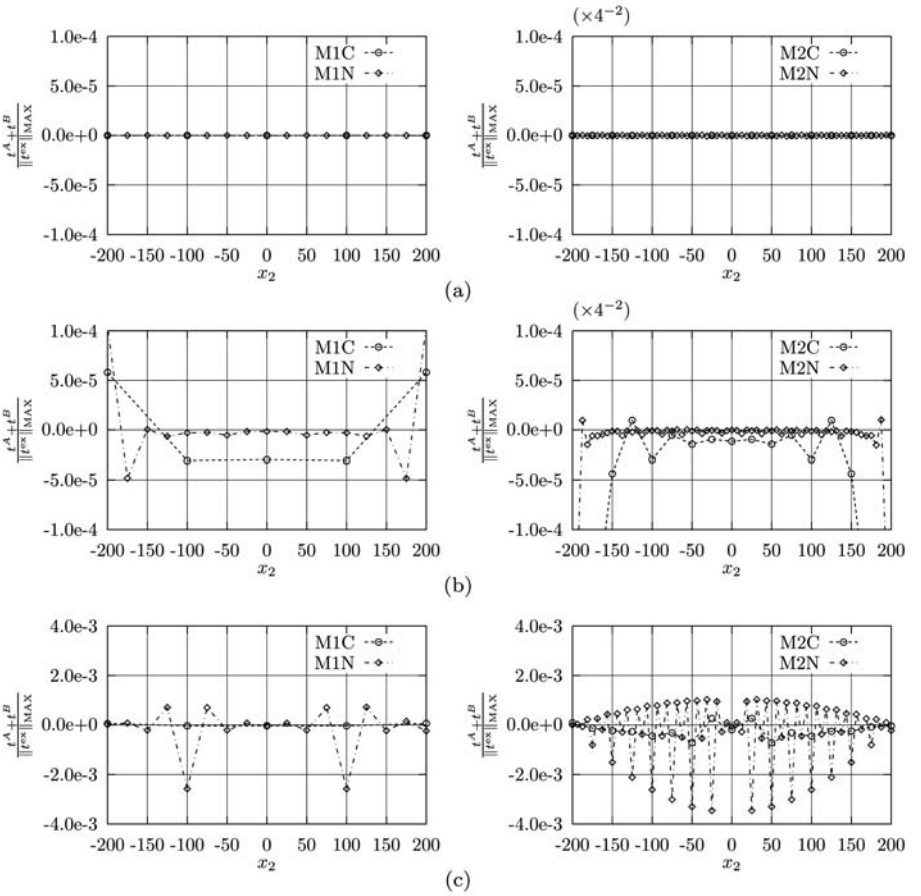

Fig. 6. Bar, simple tension problem. Traction t_1 difference along the interface, matching and non-matching meshes, (a) L, (b) A, (c) D.

All these observations keep valid for the refined meshes M2, see the right column of Figure 6. It can be observed that the data in the cases L and A have nicely converged quadratically as there is four times more elements in the finer mesh. On the contrary, though overlapping of the domains is four times less for the mesh M2, due to the different value of radius R', the magnitude of the error remains approximately the same. The oscillating character of the error distribution, caused by the different number of elements and/or their mutual position along the interface, is similar for both the coarse and the finer meshes.

Analogous observations are also valid for displacements, the right plots of Figures 5 and 7. The displacement component u_2 considered is distributed linearly

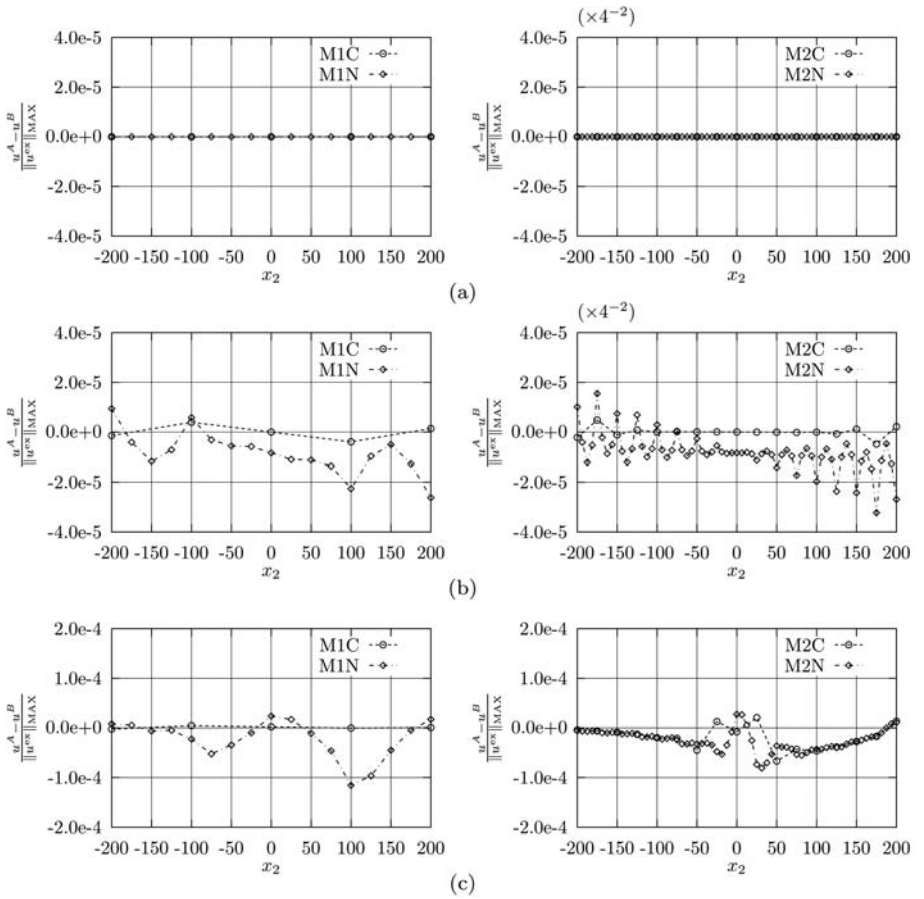

Fig. 7. Bar, simple tension problem. Displacement u_2 difference along the interface, matching and non-matching meshes, (a) L, (b) A, (c) D.

along the interface. Therefore, the error distribution and also the interface differences may exhibit some linear trend in addition to an oscillatory character of the distribution for the curved interface. In presence of geometrically non-conforming interface, the errors are significantly larger, see Figure 7(c). In particular, it could be expected that for the same number of elements on both sides (conforming mesh) of a geometrically non-conforming interface large errors may appear, the right plot of Figure 7 (c).

In the second example, transfer of a linear traction solution and a quadratic displacement solution across an interface in the pure bending problem of a beam, see Figure 2(b), is studied. The obtained data are compared with the data in the previous example.

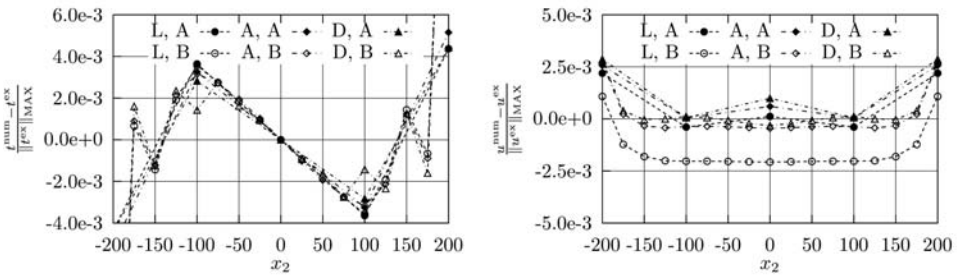

Fig. 8. Beam_V, pure bending problem. Relative errors of interface tractions t_1 and displacements u_2, mesh M1, non-matching meshes.

With reference to the traction component, t_1, it is interesting to notice that the relative errors for non-matching meshes shown in the left plot of Figure 8 are very similar for all three interface configurations. The linear distribution of the solution has a clear influence on the distribution of the errors.

The non-constant distribution of the traction also affects the distribution of the differences between the tractions t_1 evaluated on both sides of the interface, see Figure 9. In this case, no significant differences appear if the interface is changed from its original straight form to the curved one, compare the cases L and A. Even the form of the error distribution and the magnitudes of the errors obtained in the case D by using the mesh M1 are similar.

Relevant differences apear between the geometrically conforming and non-conforming interfaces, if the mesh is refined, see the plots in the right column of Figure 9. The solution is linear along the straight interface or almost linear if it is curved, thus the approximation with more linear elements, even only along one side of the interface, may provide a more accurate solution for the non-conforming mesh.

The data in the cases L and A have nicely converged quadratically as there is four times more elements in the mesh M2 than in the mesh M1. Though overlapping of the domains in the case D is four times less for the mesh M2 than for the mesh M1, in view of the different value of the radius R' used, the magnitudes of the error remains approximately the same for both meshes. The oscillating character of the error distribution copies the mesh pattern similarly to the case of the bar in tension. However, when the interface is discretized with the same number of elements, the influence of the subdomains overlapping is suppressed. Therefore, a non-conforming geometry of the interface together with non-matching meshes may lead to strong oscillations in the traction solution difference between both interface sides.

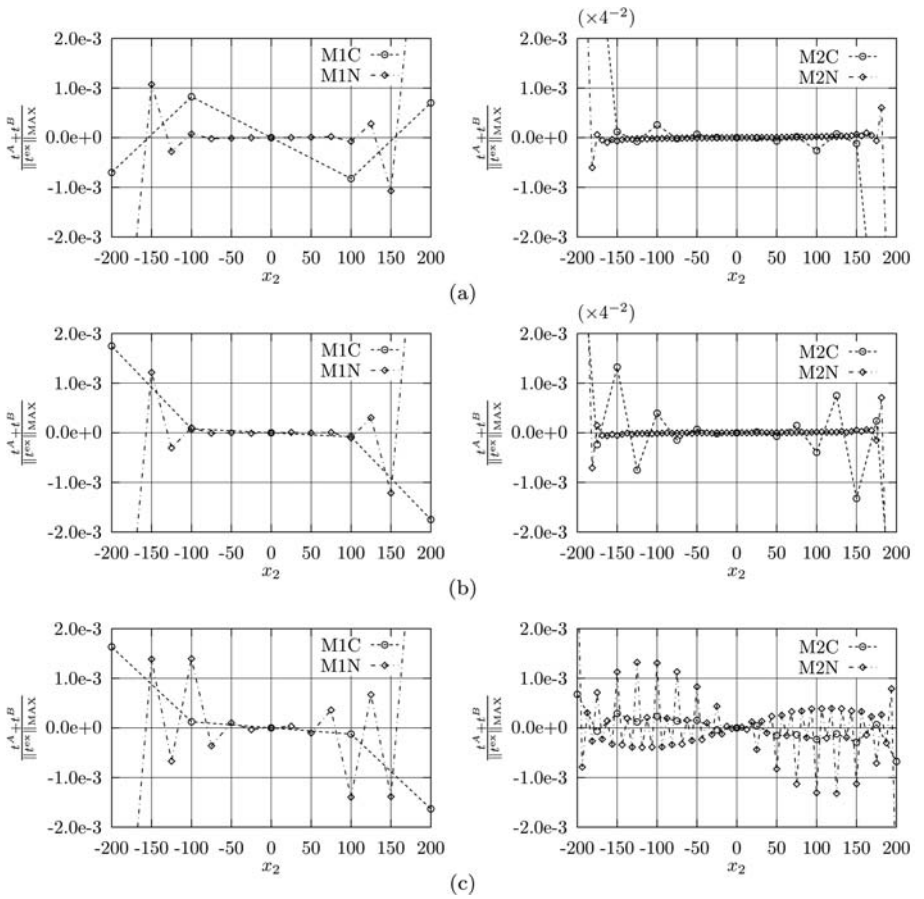

Fig. 9. Beam_V, pure bending problem. Traction t_1 difference along the interface, matching and non-matching meshes, (a) L, (b) A, (c) D.

With reference to the displacement component, u_2, the quadratic distribution of the solution has a clear influence on the error distribution shown in the right plot of Figure 8. It is also interesting to notice that the displacement errors for a curved interface are in some places smaller than those for the straight interface. The displacement u_2 differences between both interface sides, shown in Figure 10, exhibit some oscillations depending on the mesh pattern of the non-matching meshes. The convergence is quadratic in both conforming geometries, cases L and A. If the interface sides curvatures are different, the error due to this geometrical non-conformity is more significant and the errors have not decreased quadratically, though they are smaller for the mesh M2, unlike the previously discussed situations, compare Figure 10(c) with Figures 9(c) and 7(c).

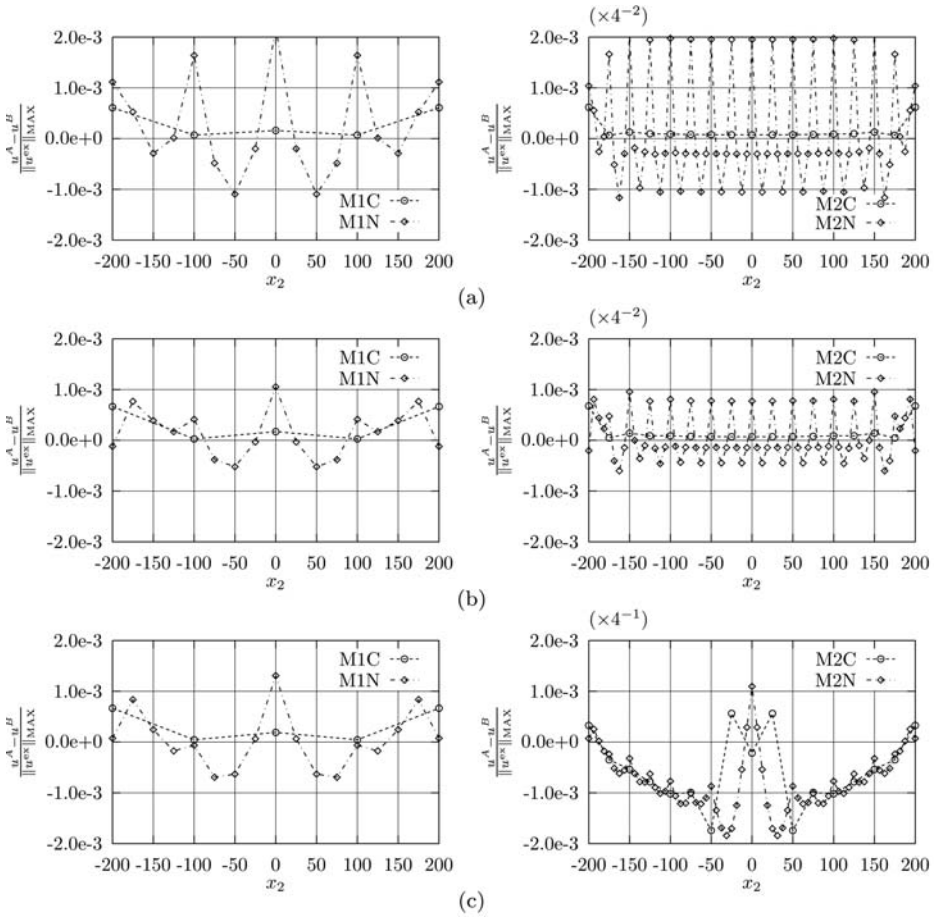

Fig. 10. Beam_V, pure bending problem. Displacement u_2 difference along the interface, matching and non-matching meshes, (a) L, (b) A, (c) D.

In the third example, the pure bending problem with the interface placed along the stress neutral axis, see Figure 2(c), is studied. Both traction components and the tangential displacement u_1 vanish on the interface, whereas the normal displacement u_2 has a quadratic distribution. Thus, the results for the traction t_1 and the displacement u_2 are presented again.

The relative errors of the traction t_1 for mesh M1, shown in the left plot of Figure 11, are smaller for the non-matching mesh than for the matching mesh, the relation observed in the previous examples sometimes. The errors are very close to zero except the interface parts close to the subdomain corners as could be expected.

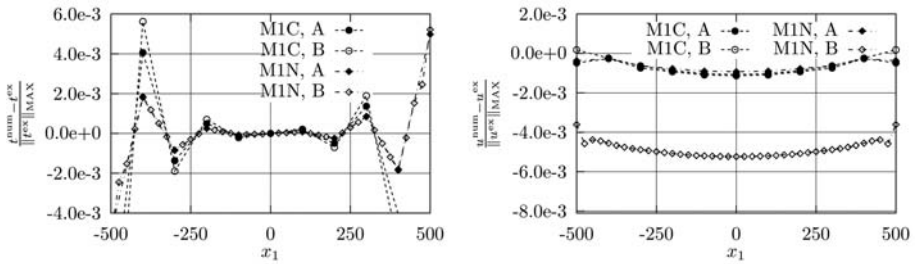

Fig. 11. Beam_L, pure bending problem. Relative errors of interface tractions t_1 and displacements u_2, mesh M1, matching and non-matching meshes.

The differences of tractions t_1 plotted in Figure 12(a) follow the behaviour of errors and have nicely converged for both matching and non-matching finer meshes.

The relative errors of displacement u_2, shown in the right plot of Figure 11, clearly follow the quadratic distribution of the displacement solution. The differences of displacements u_2 plotted in Figure 12(b) have nicely converged both for matching and non-matching finer meshes, and are very small for matching meshes. In addition, the pattern oscillation, similar to that observed in the previous Beam_V case, confirms the fact, see [**17**], that the displacements pertinent to the

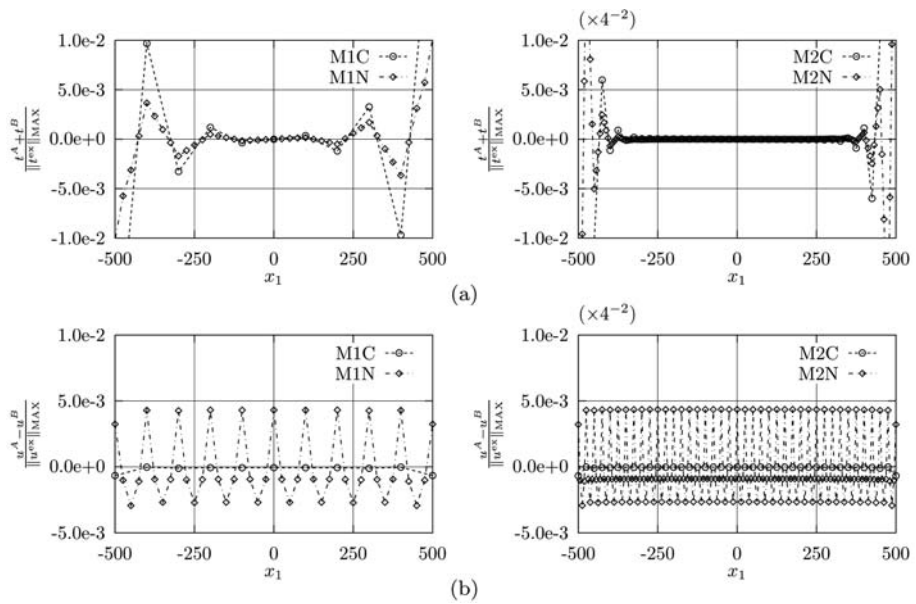

Fig. 12. Beam_L, pure bending problem. Traction t_1 and displacement u_2 difference along the interface, matching and non-matching meshes, (a) tractions, (b) displacements.

domain Ω^B are calculated first in the numerical solution so that they obey the quadratic solution. Transferring them to the coarser mesh by using a linear interpolation between its nodes may produce exactly the type of oscillatory behaviour shown in Figure 12(b).

5.4 - *Tests with dissimilar materials*

The analysis of the numerical results obtained in the inclusion-matrix problem is focused on the interface again. Note that, taking into account the analysis introduced in [**17**], the inclusion and matrix correspond to the subdomains Ω^A and Ω^B, respectively, and the fine mesh is always defined on the matrix side. The analytical solution is smooth, and also there are no end points of the interface to perturb the solution. Thus, the errors are basically influenced by the type of meshing, see Figure 13, the angle φ being defined in Figure 4. The only data which have non-smooth distribution of the error belong to the finer mesh of the non-matching mesh distribution. However, this is not caused by the dissimilar materials considered, as the same character of the error distribution are observed also when both materials of the subdomains are the same, see [**17**]. Notice that the displacement results for the non-matching meshes have been plotted in a different scale in order to see not only the difference between the matching and non-matching meshes, but also the actual error distribution in the case of matching meshes.

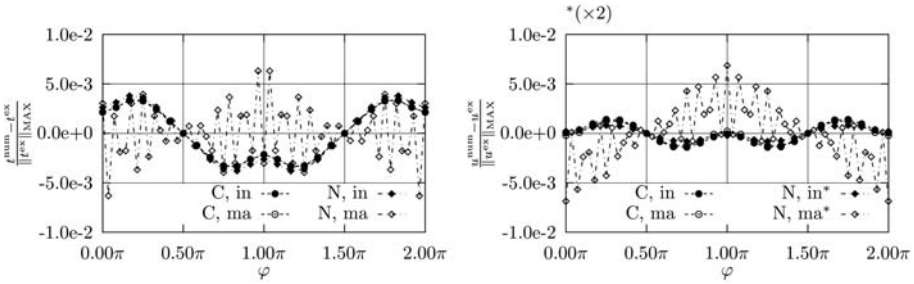

Fig. 13. Inclusion-matrix problem, glass-epoxy. Relative errors of interface tractions t_1 and displacements u_1, mesh M2, matching and non-matching meshes.

The solution difference between both sides of the interface, shown in Figure 14, does not provide any additional information on the behaviour of the numerical results, the oscillations observed for the non-matching mesh being given by the oscillations of the errors on the finer mesh.

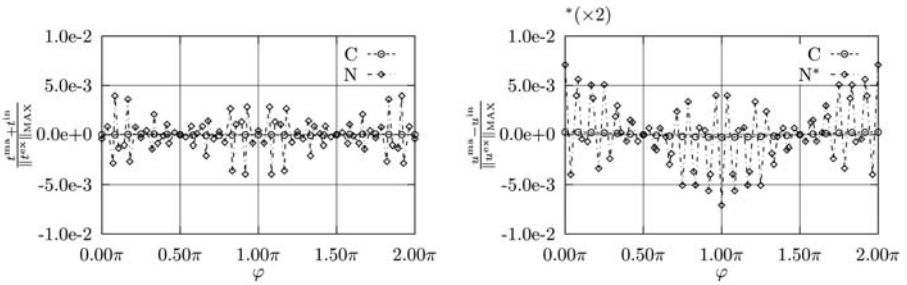

Fig. 14. Inclusion-matrix problem, glass-epoxy. Traction t_1 and displacement u_1 difference along the interface, mesh M2, matching and non-matching meshes.

It is expected that the norm of the relative error obeys the quadratic convergence rule. The norms defined in Section 5.2 are used to check this error convergence behaviour. The dependences of the relative error norms on the characteristic number of the elements at the interface $N = \min(N^A, N^B)$ (N^A and N^B are the numbers of the elements on the two sides of the interface defined by Ω^A and Ω^B, respectively) are plotted for tractions and displacements in Figure 15.

The satisfactory result is that in both norms the convergence rate obtained is quadratic as expected. Numerical values of the estimated fitting parameters

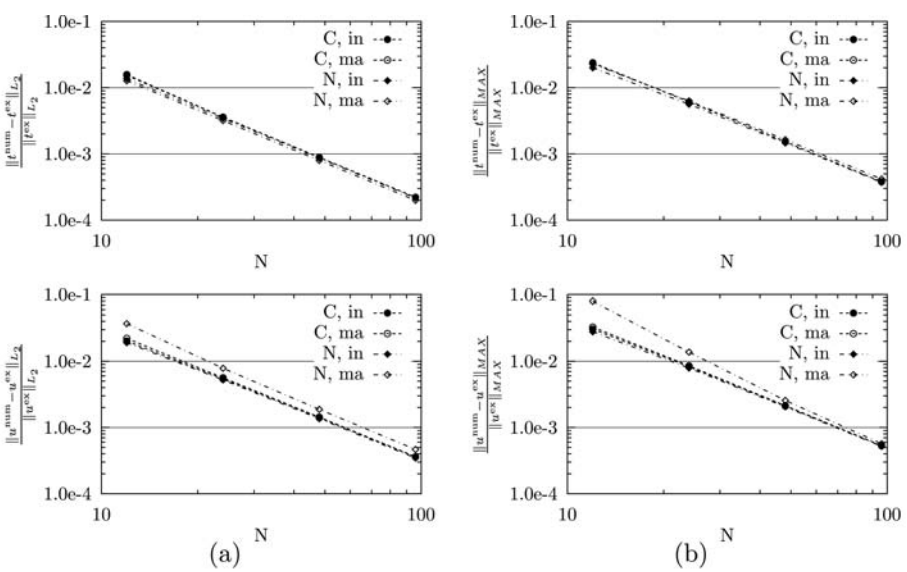

Fig. 15. Inclusion-matrix problem, glass-epoxy. Interface traction and displacement error convergence, matching and non-matching meshes, (a) L_2 norm, (b) MAX norm.

from the regression analysis are summarized in Table 1. The power dependence is actually significant already for these initial refinements of the mesh due to the high correlation coefficient r. The parameter β is close to the expected value of 2 with an exception of the bottom right corner of the table. However, the curve corresponding to this exception is approaching the other curves, see Figure 15, so this exception seems to be associated to the initial refinements with relatively coarse meshes only.

Table 1. *Inclusion-matrix problem, glass-epoxy. Error convergence rates, matching and non-matching meshes.*

$\|\cdot\| = qN^{-\beta}$		L_2		MAX	
		$\boldsymbol{t}$	$\boldsymbol{u}$	$\boldsymbol{t}$	$\boldsymbol{u}$
C, in	β	2.0087	1.9569	1.9913	1.9531
	q	2.1196	2.7207	3.3817	4.0032
	r^2	0.9997	0.9999	1.0000	0.9998
C, ma	β	2.0065	1.9809	1.9857	1.9824
	q	2.1013	3.0593	3.3113	4.5753
	r^2	0.9999	1.0000	0.9999	0.9999
N, in	β	1.9975	1.9610	1.9186	1.9183
	q	1.9596	2.6712	2.4149	3.3755
	r^2	1.0000	0.9998	0.9997	0.9996
N, ma	β	1.9982	2.0378	1.9235	2.3832
	q	1.8179	5.0620	2.7644	28.1159
	r^2	1.0000	0.9994	0.9998	0.9987

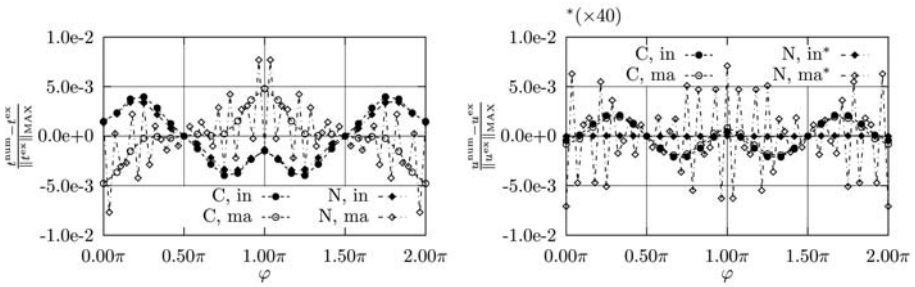

Fig. 16. Inclusion-matrix problem, limit parameters. Relative errors of interface tractions t_1 and displacements u_1, mesh M2, matching and non-matching meshes.

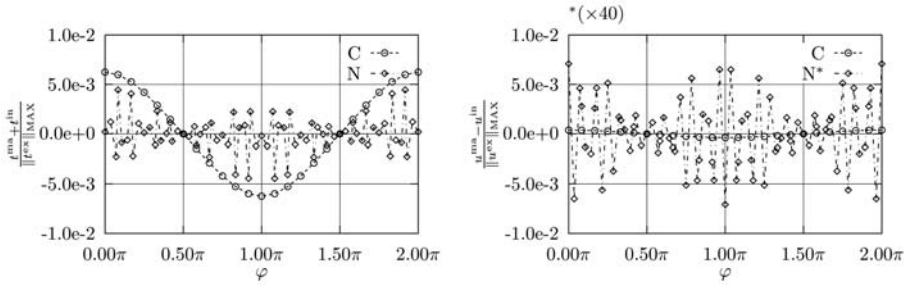

Fig. 17. Inclusion-matrix problem, limit parameters. Traction t_1 and displacement u_1 difference along the interface, mesh M2.

All the previous observations remain valid also for the limit case of material properties. The plots in the following figures can be compared in this sense: Figure 13 with 16, Figure 14 with 17 and Figure 15 with 18. All distributions seem to be very similar, except for the interface tractions for the matching mesh and a more important error for displacements obtained in the non-matching case (the used factor here is 40 instead of 2). The value of the Poisson ratio of the matrix is the source of these differences. Its value 0.499 is rather close to one half – the limit for an incompressible material.

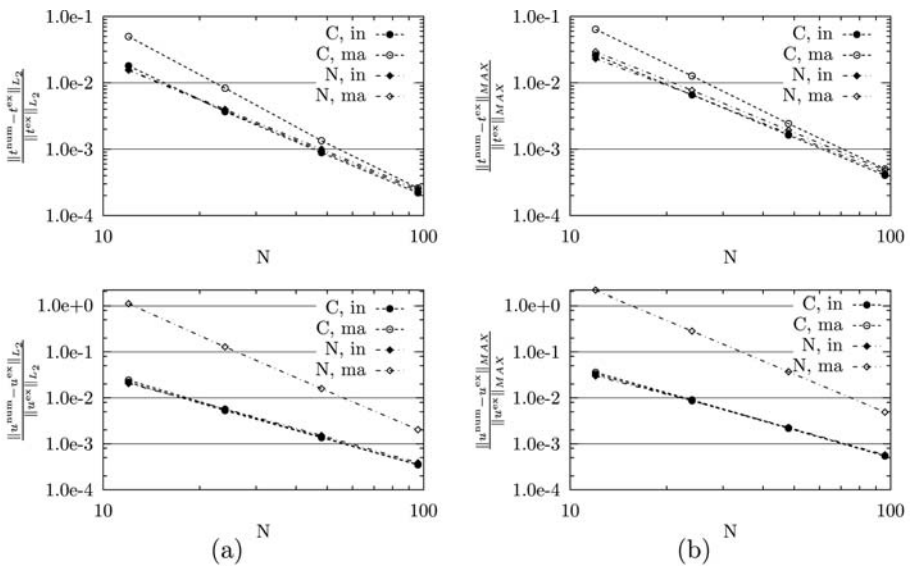

Fig. 18. Inclusion-matrix problem, limit parameters. Interface traction and displacement error convergence, matching and non-matching meshes, (a) L_2 norm, (b) MAX norm.

Table 2. *Inclusion-matrix problem, limit parameters. Error convergence rates, matching and non-matching meshes.*

$\|\cdot\| = qN^{-\beta}$		L_2		MAX	
		$\boldsymbol{t}$	$\boldsymbol{u}$	$\boldsymbol{t}$	$\boldsymbol{u}$
C, in	β	2.1131	1.9867	2.0069	1.9733
	q	3.2496	2.9899	3.8489	4.4814
	r^2	0.9990	0.9999	1.0000	0.9999
C, ma	β	2.5370	2.0303	2.3353	2.0124
	q	26.4942	3.6784	21.0845	5.3600
	r^2	0.9995	0.9998	0.9999	1.0000
N, in	β	1.9887	1.9109	1.9114	1.9016
	q	2.2046	2.4268	2.7591	3.4864
	r^2	1.0000	0.9997	0.9995	0.9995
N, ma	β	2.0135	3.0317	1.9791	2.9265
	q	2.2891	2030.2609	4.0696	3090.2166
	r^2	1.0000	0.9999	0.9999	1.0000

Numerical values of the estimated fitting parameters from the regression analysis of the error convergence behaviour are summarized in Table 2. The power dependence is not perturbed when looking at the values of the correlation coefficient r. Also the parameter β is more or less close to its expected value of 2, the exceptions correspond to the above described differences between the two bi-material cases. Nevertheless, the refinements of the mesh not only improve the errors but also make the results similar to the example with more realistic material parameters (glass-epoxy).

6 - Conclusions

Two variational formulations of the SGBEM for DDBVPs were introduced, both of them leading to the same discretized system. Though the origin of both formulations is different, one of them is domain based, and the other is completely boundary based, the relation between the corresponding functionals can be deduced. This relation was presented in [**19**].

The present SGBEM approach applied to a Domain Decomposition BVP has been numerically tested to characterize its behaviour for particular kinds of problems which may involve some features making the numerical solution more difficult. First, the fulfillment of the compatibility and equilibrium of the interface

displacements and tractions, respectively, are analyzed. Simple test examples, including simple tension and pure bending problems, similar to those used in finite element patch tests have been chosen: the unknown interface tractions are either constant or linear with linear or quadratic distribution of interface displacements. As follows from the numerical results obtained, while the character of the unknown solution distribution is the same as the order of boundary element approximation, the solution transferred across the interface is satisfactorily accurate. This remains also valid if the interface is slightly perturbed but geometrically conforming, although the non-matching boundary element meshes may lead to some small overlapping of the discretized subdomains. However, a care must be taken when the neighbourhood subdomains are actually geometrically non-conforming.

Another series of test examples includes a smooth and closed curved interface between dissimilar materials. When the results are compared with the previously presented data obtained from an analysis with the same materials [**17**], no substantial difference in the numerical behaviour has been observed. Naturally, with the material parameters pushed to their possible limit values some exceptions may occur, however, this is not the problem of the present approach only.

The convergence of the method for h-refinements has also been studied here for the case of bi-material interfaces using the discretized L_2 and maximum norms of error. The quadratic rate of convergence in both norms has been obtained for both tractions and displacements as could be expected for linear elements and for smooth closed interfaces, see [**17**]. According to the authors experience, in presence of the end-points at the interface (corners of the adjacent subdomains) the obtained results may converge worse in traction error norms, including the matching mesh case. This phenomenon has not been tested explicitly with dissimilar materials, but it can be expected according to the data obtained in the first series of examples.

A modification of the present SGBEM approach for DDBVP in relation to the definition of interface conditions can include Lagrange multipliers, which might modify some of the conclusions presented. Such a new approach using additional interface unknowns has recently been introduced by the present authors in [**18**].

Acknowledgments. The authors acknowledge support by the grant (R.V.) VEGA No. 1/0673/10. The institution of R.V. is also supported in the frame of the operational programme *Research and Development* coordinated by the Ministry of Education of the Slovak Republic under the call OPVaV-2008/2.1/01-SORO (ITMS: 26220120018). The other financial support has been given to V.M. from the Junta de Andalucía (Project of Excellence P08-TEP-04051).

References

[1] A. Blázquez, F. París and V. Mantič, *BEM solution of two-dimensional contact problems by weak application of contact conditions with non-conforming discretizations*, Internat. J. Solids Structures **35** (1998), 3259-3278.

[2] M. Bonnet, *Regularized direct and indirect symmetric variational BIE formulations for three-dimensional elasticity*, Eng. Anal. Bound. Elem. **15** (1995), 93-102.

[3] M. Bonnet, G. Maier and C. Polizzotto, *Symmetric Galerkin boundary element methods*, Appl. Mech. Rev. **51** (1998), 669-704.

[4] M. A. Crisfield, *Re-visiting the contact patch test*, Internat. J. Numer. Methods Engrg. **48** (2000), 435-449.

[5] L. J. Gray and G. H. Paulino, *Symmetric Galerkin boundary integral formulation for interface and multi-zone problems*, Internat. J. Numer. Methods Engrg. **40** (1997), 3085-3101.

[6] G. C. Hsiao, O. Steinbach and W. L. Wendland, *Domain decomposition methods via boundary integral equations*, J. Comput. Appl. Math. **125** (2000), 521-537.

[7] L. F. Kallivokas, T. Juneja and J. Bielak, *A symmetric Galerkin BEM variational framework for multi-domain interface problems*, Comput. Methods Appl. Mech. Engrg. **194** (2005), 3607-3636.

[8] T. A. Laursen and M. W. Heinstein, *Consistent mesh tying methods for topologically distinct discretized surfaces in non-linear solid mechanics*, Internat. J. Numer. Methods Engrg. **57** (2003), 1197-1242.

[9] G. Maier, M. Diligenti and A. Carini, *A variational approach to boundary element elastodynamic analysis and extension to multidomain problems*, Comput. Methods Appl. Mech. Engrg. **92** (1991), 193-213.

[10] V. Mantič, *Computer implementation of the boundary element method with multilevel substructuring*, PhD thesis, TU Košice, Faculty of mechanical engineering, 1992.

[11] J. P. Núñez, D. Muñoz, V. Mantič and F. París, *A weak application of transmission conditions in 2D BEM with non-conforming meshes for isotropic and anisotropic potential problems*, in "Advances in Boundary Element Techniques IV", R. Gallego and M. H. Aliabadi, eds., Queen Mary, University of London, London 2003, 111-116.

[12] T. Panzeca, M. Salerno and S. Terravecchia, *Domain decomposition in the symmetric boundary element analysis*, Comput. Mech. **28** (2002), 191-201.

[13] F. París and J. Cañas, *Boundary element method. Fundamentals and applications*, Oxford University Press, New York 1997.

[14] C. Polizzotto, *A boundary min-max principle as a tool for boundary element formulations*, Eng. Anal. Bound. Elem. **8** (1991), 89-93.

[15] T. Rüberg and M. Schanz, *Coupling finite and boundary element methods for static and dynamic elastic problems with non-conforming interfaces*, Comput. Methods Appl. Mech. Engrg. **198** (2008), 449-458.

[16] A. Sutradhar, G. H. Paulino and L. J. Gray, *Symmetric Galerkin boundary element method*, Springer-Verlag, Berlin 2008.

[**17**] R. VODIČKA, V. MANTIČ and F. PARÍS, *Symmetric variational formulation of BIE for domain decomposition problems in elasticity - An SGBEM approach for nonconforming discretizations of curved interfaces*, CMES Comput. Model. Eng. Sci. **17** (2007), 173-203.

[**18**] R. VODIČKA, V. MANTIČ and F. PARÍS, *SGBEM with Lagrange multipliers applied to elastic domain decomposition problems with curved interfaces using non-matching meshes*, Internat. J. Numer. Methods Engrg. **83** (2010), 91-128.

[**19**] R. VODIČKA, V. MANTIČ and F. PARÍS, *Two variational formulations for elastic domain decomposition problems solved by SGBEM enforcing coupling conditions in a weak form*, Eng. Anal. Bound. Elem. **35** (2011), 148-155.

[**20**] J. N. GOODIER, *Concentration of stress around spherical and cylindrical inclusions and flaws*, Trans. ASME J. Appl. Mech. **55** (1933), 39-44.

[**21**] V. MANTIČ, *Interface crack onset at a circular cylindrical inclusion under a remote transverse tension. Application of a coupled stress and energy criterion*, Internat. J. Solids Structures **46** (2009), 1287-1304.

ROMAN VODIČKA
Technical University of Košice
Civil Engineering Faculty
Vysokoškolská 4
Košice, 042 00, Slovakia
e-mail: roman.vodicka@tuke.sk

VLADISLAV MANTIČ
University of Seville
School of Engineering
Camino de los Descubrimientos s/n
Seville, 41092, Spain
e-mail: mantic@esi.us.es